# Effect of different source terms in atmospheric boundary modelling over the complex terrain site of Perdigao

Kartik Venkatraman[1,2,*], Trond-Ola Hågbo[1,3,*], Sophia Buckingham[1], and Knut Erik Teigen Giljarhus[3]

[1]von Karman Institute for Fluid Dynamics, Waterloosesteenweg 72, B-1640 Sint-Genesius-Rode, Belgium
[2]Université de Sherbrooke, Canada
[3]University of Stavanger, Norway
[*]These authors contributed equally to this work.

**Correspondence:** kartik.venkatraman@vki.ac.be

**Abstract.** The assessment of wind conditions in complex terrain requires ~~the use of~~ Computational Fluid Dynamics (CFD) simulations incorporating an accurate parameterization of forest canopy effects and ~~variable thermal stability~~ Coriolis effects. This study ~~aims to investigate how incorporating~~ investigates how incorporating source terms such as the presence of trees ~~can improve the~~ and the Coriolis force can improve flow predictions. Furthermore, the study examines the impact of using different sets of atmospheric boundary layer inflow profiles, including idealized profiles with a logarithmic velocity profile, and a set of fully developed profiles from a pressure-driven precursor simulation. A three-dimensional steady Reynolds-averaged Navier-Stokes (RANS) equations model is set up using OpenFOAM to simulate the flow over a complex terrain site comprising two parallel ridges ~~located~~ near Perdigão, Portugal. A 7.5 km × 7.5 km terrain of the Perdigao site is constructed from elevation data centered around a 100 m met-mast located on the ~~northeast~~ Southwest ridge. A 30-min averaged stationary period ~~corresponding~~ is simulated, which corresponds to near-neutral conditions ~~on a single~~ at met-mast ~~tower is simulated. The impact of incorporating different source terms is studied such as forest canopy, Coriolis forces as well as also buoyancy forces~~ Tower 20 located at the Southwest ridge. The period corresponds to the wind is coming from Southwest at 231° at 100 m height above ground at Tower 20. Five different case setups are simulated using a combination different source terms, turbulence models and inflow profiles. The prediction capability of ~~the~~ these models is analyzed for different groups of towers on the ~~South-West ridge ,~~ Southwest ridge and on the towers further downstream inside the valley, and on the ~~North-East ridgebased on the flow topology~~ Northeast ridge. The inclusion of a canopy model ~~is shown to improve~~ improves predictions close to the ground for most of the towers ~~, while reducing prediction accuracy on top of the ridges, illustrating the need to represent terrain heterogeneity~~ on the Southwest ridge and inside the valley. Large uncertainties are seen in field measurement data inside the valley, which is a re-circulation zone and large prediction errors are seen in the wind velocity, wind direction and turbulent kinetic profiles for most of the models. The predictions on the Northeast ridge is dependent on the extent of re-circulation predicted inside the valley. The precursor inflow model provides the best match for the wind velocity at Tower 29 on the Northeast ridge, while the canopy model shows a large under prediction.

# 1 Introduction

Lack of terrain availability in flat terrain pushes wind-farm developers to look for ~~alternative sites along complex terrains~~alternatives
along complex terrain sites. Flat terrain availability is becoming scarce and 70% of the Earth's surface is in complex terrain,
which presents large potential for wind energy harvesting. Winds in complex terrains are governed by the surface properties of
the flow (land class/roughness) and the local elevation such as hills, ridges and mountains ~~(Emeis, 2018)~~(Emeis 2018). Local
features such as ridges or canyons can also be advantageous for wind energy harvesting, due to the creation of local flow
accelerations on top of ridges and flow channeling through valleys. However, the wind fields are dependent on either the local
pressure or temperature gradient. Such flows are also dominated by strong thermal stratification effects and are influenced by
presence of forest canopies. Complex ~~terrains~~ terrain sites remain very challenging areas to consider for wind farm siting and
require extensive validation of modeling tools in representative environments. Wind farm modeling for complex terrains re-
quires a more advanced approach than commonly used cost-effective linearized models such as WAsP ( Jørgensen et al., 2005)
which cannot handle complex phenomena (i.e. flow separation) to ensure reliable and accurate results. Computational fluid
dynamics (CFD) tools are increasingly used to predict flows over complex ~~terrains~~ terrain sites to account for such phenomena
and provide more ~~reliable~~ accurate wind resource predictions (Blocken, 2014). However, improving numerical modeling tools
for complex terrains demands accounting for various microscale phenomena such as flow re-circulation and the forest canopy
effect. Such microscale flow features have a significant impact on local wind resource assessment and wind turbine loading.

Inital studies in literature accounting for effects of forest canopy were performed over forested flat terrains. Brower (2012)
showed that the presence of a forest canopy increases the modelling uncertainty by up to a factor of 5 irrespective of the chosen
modelling approach. Finnigan (2000) parameterized the effect of foliage and forest canopy by accounting for the drag force in
the momentum equation. The effect of canopy on turbulence was further taken into account by Sogachev and Panfyorov (2006)
and Sogachev (2009) by adding additional source terms for turbulence kinetic energy and turbulence dissipation rate. Desmond
et al. (2017) modelled both forest canopy and buoyancy effects by modelling them using source and sink terms and showed that
the thermal stratification plays an important role in determining the flow over canopies. The canopy model is typically imple-
mented by specifying the tree height and leaf area density (LAD), which represents the area of the leaf and branches of trees.
These parameters are typically defined from field measurements or LiDAR point clouds generated from field measurement
campaigns and aerial surveys (Queck et al., 2012).

Validation of numerical models for complex terrains requires field measurements. One of the earliest field campaigns was
at Askervin hill (Salmon et al., 1988), which is a smooth isolated hill. Similarly, the Bolund hill campaign was another
campaign over an isolated hill in Denmark ~~(Bechmann et al., 2009)~~ as detailed by Bechmann et al. (2009), with data un-
der conditions which could be classified as neutral. However no canopy is seen on these sites. The Alaiz field campaign
~~(Rodrigo et al., 2021)~~ was performed over a large scale homogeneous mountain valley topography in Spain with forested re-
gions (Rodrigo et al., 2021). Chavez et al. (2014) showed that using a canopy model improved the accuracy of velocity and
turbulence predictions for simulations over Alaiz.

More recently, a field experiment campaign has been carried out over the complex terrain ~~terrain~~ site at Perdigão, Portugal, by (Fernando et al., 2018) which is a double ridge with forested canopy experiencing different thermal stratification conditions. Significant field data is available for further studies~~and is further~~, and these are elaborated in Section 2. Several numerical studies have been performed for validation with field data. Laginha Palma et al. (2020) studied the choice of using the appropriate grid size for numerical modelling. Wagner et al. (2019) implemented a forest parameterization in the Weather Research and Forecasting model (WRF) with an average tree height of 30 m, resulting in an improvement in prediction of near surface wind speeds. This was chosen due to practical reasons related to the model setup and is not representative of actual tree height. There is a gap in existing literature on microscale simulations using a canopy model on a heterogeneous forested complex terrain with a rich dataset such as Perdigão. ~~This study aims to address that research gap by investigation of the effect of specific microscale effects related to the modeling of trees and buoyancy effects at the complex terrain test-case of Perdigão at several met-mast locations and to verify if the forest parameterization helps improve predictions using a RANS simulation approach.~~

## 1.1 Objectives and outline

This paper aims to evaluate the impact of different physical source terms and turbulence models when performing CFD simulations in complex terrain and compare simulation prediction with field measurement profiles at the different groups of towers located at the Perdigão test site. The influence of the following parameters are investigated: Canopy effects, Coriolis force, ~~impact of non-neutral effects (buoyancy forces).~~ and the effect of using two different sets of inflow profiles. One idealized set with a log-law velocity profile, and one set of fully developed profiles based on a precursor simulation.

An improved understanding of the importance of these phenomena will enable development of more efficient and reliable tools to perform wind simulations in complex terrain. This paper is structured as follows: a detailed description of the methodology is provided in Section 2, covering the computational domain and meshing, the numerical settings and different modeling capabilities that have been added as source terms to the conservation equations. The results are presented and discussed in Section 3, in terms of different groups of towers. Section 4 is dedicated to concluding remarks and future perspectives.

## 2 Perdigão Field measurement campaign

An intensive observation period was carried out from 1 May 2017 to 15 June 2017 at the double ridge site of Perdigão, Portugal, by a consortium of American & European universities (Fernando et al. 2018). The location of the different met masts of heights 60 m and 100 m used in this study is shown in Fig. 2, which could be grouped by their location on top of the ~~South-West~~ Southwest ridge, inside the valley, or at top of the ~~North-East~~ Northeast ridge. From the analysis of the wind rose, the predominant directions at Tower 20 and Tower 29 are perpendicular to the ridges, i.e ~~North-East and South-West~~ Northeast and Southwest directions, as shown in Fig. 1, while at Tower 25, flow turning is seen and the dominant wind direction is from the South.

(a) Tower 20 (tse04).     (b) Tower 25 (tse09).     (c) Tower 29 (tse13).
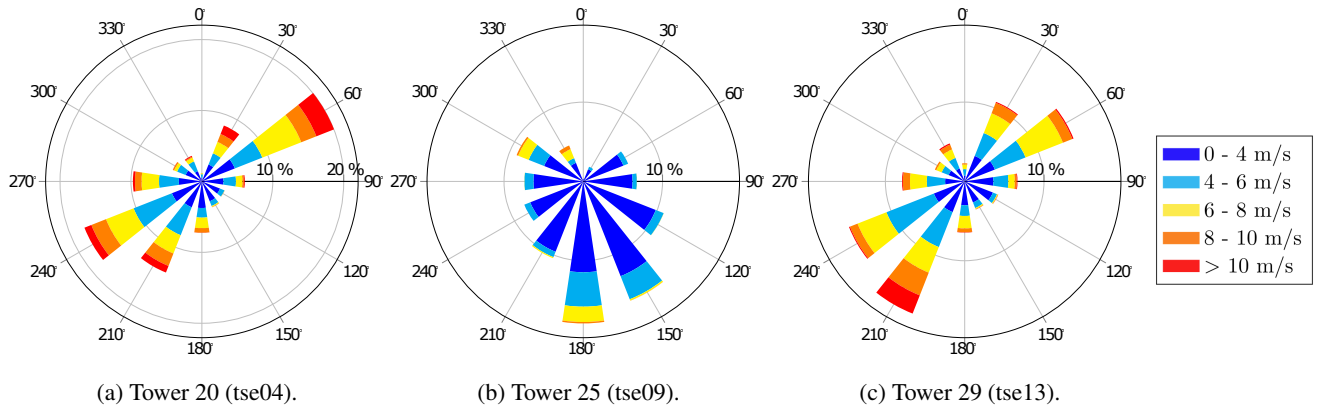
**Figure 1.** Wind rose for 1 month period of May 2017 for towers on top of the ridges and inside the valley.
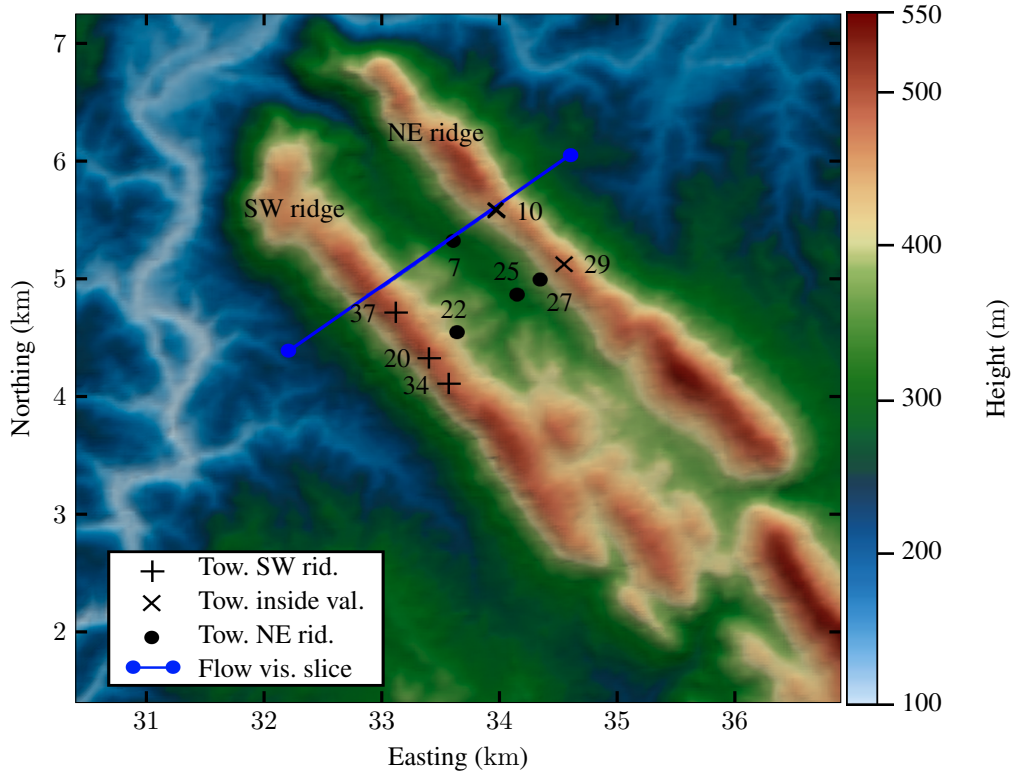
**Figure 2.** Elevation map and locations of interest at Perdigao. Positions of the measurements towers in the SW ridge group are indicated with + symbols, likewise are NE masts marked with x, and the masts in the inside valley group are indicated with black dots. The blue dots and the line represents the flow visualization slice used in Fig. 15. PT-TM06/ETRS89 coordinate system, height above sea level.

A stationary period was found on the date of 4th May, 2017 for the 30 minute averaged time interval of $22:00 - 22:30$ tilt corrected high frequency dataset from NCAR-EOL, based on the conditions at Tower 20 on top of the ridge, which cor-

responded to a ~~bulk~~ Bulk Richardson number of approximately -0.03 which qualifies as near-neutral condition. The ~~bulk~~
~~Richardson number (Kaimal and Finnigan, 1994)~~ Bulk Richardson number as defined by Kaimal and Finnigan (1994) is cal-
culated using Eqn. 1. However, the flow conditions are non-neutral at other met mast locations.

$$Ri_b = \frac{g(\bar{\theta_{100}} - \bar{\theta}_2)\Delta z}{\bar{\theta}_{100}[U_{100}^2 + V_{100}^2]} \tag{1}$$

where $\theta$ is the potential temperature, $g$ is the acceleration due to gravity, $U, V$ are the wind velocity components at the
reference height (m). The same period was simulated by Laginha Palma et al. (2020) based on the stationary periods predicted
by Carvalho (2019).

## 3 Methodology

The terrain is a $7.5\,\mathrm{km} \times 7.5\,\mathrm{km}$ square centralized around a $100\,\mathrm{m}$ met-mast located on the ~~south-west~~ Southwest ridge. Fig. 3
presents the computational domain and the dimensions are listed on the right side of the figure.

$H = 10 \times \Delta h_t = 4.4\,\mathrm{km}$
$R = 11.9\,\mathrm{km}$
$d_1 = 3.8\,\mathrm{km}$
$d_2 = 15 \times \Delta h_t = 6.6\,\mathrm{km}$
$\Delta h_t = 440\,\mathrm{m}$
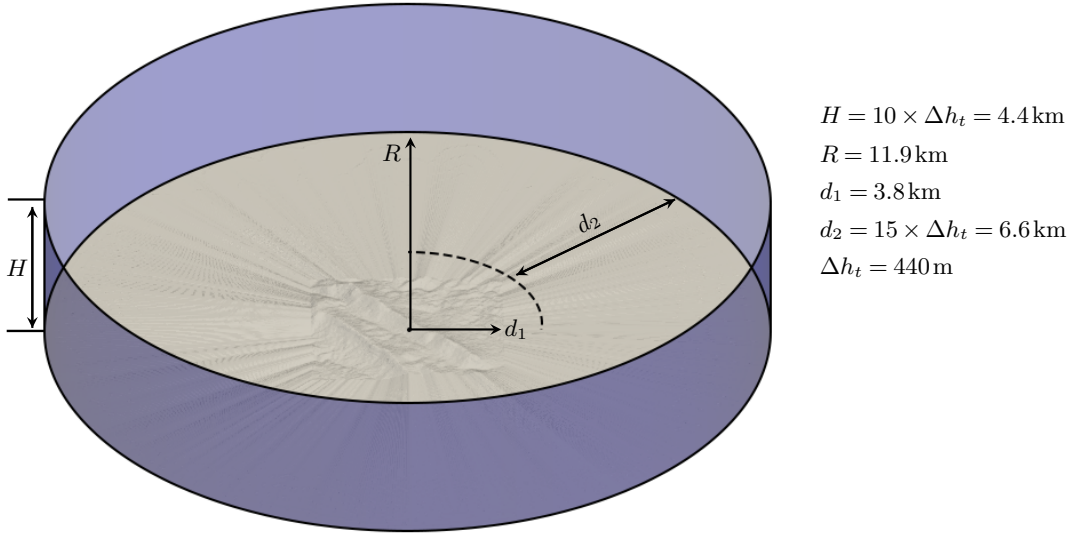
**Figure 3.** Computational domain, $\Delta h_t$ is the difference in the elevation height of the terrain.

A cylindrical computation domain was developed, which provides the flexibility to simulate wind from any wind direc-
tion. This approach has also been successfully applied by the authors in a previous study pertaining to urban areas (Hågbo
et al. 2020). A smoothing region from complex to flat terrain was applied towards the outer boundaries, with a minimum
radial distance of 15 $\Delta h_t$. Several best practice guidelines have been formulated for grid generation for simulating complex
~~terrains~~terrain sites, such as by Sørensen et al. (2012) and Laginha Palma et al. (2020) and have been closely followed. The
height of the domain is set to ten times the difference in the elevation height of the terrain, $\Delta h_t$, as recommended by Sørensen

et al. (2012) when simulating wind flow over complex terrain sites. It consists of 12.7 million cells and is produced with `terrainBlockMesher` developed by (Schmidt et al., 2012), capable of generating structured meshes over complex terrain exclusively consisting of hexahedra cells. The `terrainBlockMesher` tool uses a blending function to smooth the transition from the terrain patch to the outer cylindrical block. Around 50 radial block cells are defined and a radial grading factor is used to enable a stretching in the horizontal direction to cluster cells across the centre of the domain and expanding towards the boundaries. In terms of the number of cells per main direction ($N_x \times N_y \times N_z$) the mesh comprises of 227 x 227 x 120 across the terrain patch. The vertical mesh resolution is 33 m with uniform stretching applied. The minimal mesh height $\Delta z$ next to the ground is close to 3 m. The mesh also follows the recommendation for having at least three cells from the ground to the height at the first sampling point for comparison with field measurements. The horizontal mesh resolution over the terrain was set close to 33 m. It satisfies the minimum resolution of 40 m recommended specifically for the Perdigão site by Laginha Palma et al. ( 2020). Fig. 4 illustrates the grid structure used inside the domain from the side. Terrestrial data was obtained from the Shuttle Radar Topography Mission (SRTM) database of the Perdigão field experiment (Fernando et al. 2018). A mesh sensitivity study was performed and is presented in the Appendix . The grid resolution is sufficiently high and for the predictions in the area of interest close to the ridges where no significant changes were observed. However, increasing the refinement close to the ground has an impact on the predictions at met-mast locations close to the ground.

All simulations have been conducted using the OpenFOAM (version 2012) toolbox. The simulations are steady-state and performed by solving the incompressible, three-dimensional steady Reynolds-averaged Navier-Stokes (RANS) equations with the finite volume method. Second-order discretization schemes were used for the spatial discretization. The initial iterative convergence criteria were that the scaled residuals should drop four orders of magnitude for all flow variables as per the BPGs. Two steady-state solvers for turbulent flow of incompressible fluids have been used: `simpleFoam` (SF) and `buoyantBoussinesqSimpleFoam` (BBSF). All thermal effects are neglected in the simulations using both the solvers, such that the atmospheric stability of the simulated atmosphere is always neutral. In these simulations, the air density is assumed constant, and the gravitational force is neglected. The BBSF solver is capable of simulating the effect of buoyancy forces, but these source terms are set to zero for the present neutral case. However, in addition to solving the continuity equation and the momentum equation, which is solved using SF, the energy equation is also included, which allows for the modeling of non-neutral atmospheric conditions.
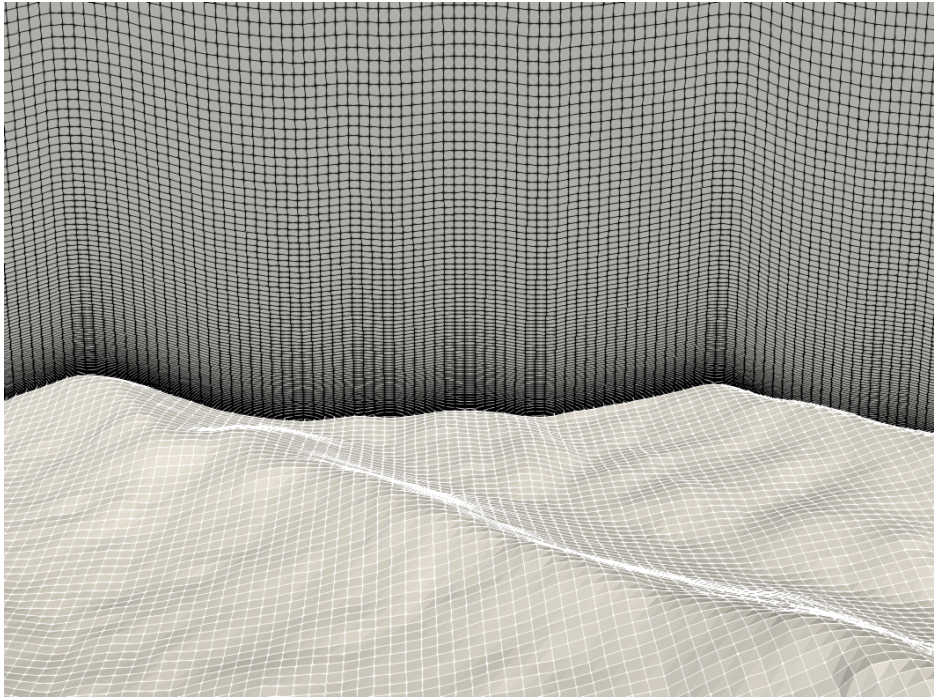
**Figure 4.** Computational grid structure, partial view from the side.

## 3.1 Inlet profiles and ~~Boundary~~ boundary conditions

Two sets of fixed inlet profiles have been used, both forming a homogeneous atmospheric boundary layer (ABL) ~~.~~ either idealized with a logarithmic velocity profile or fully developed profiles obtained from a precursor simulation. ~~The precursor~~

140  ~~model is further described by Alletto et al. (2018) and Koblitz (2013).~~

The idealized profiles provide the turbulence quantities and a log-law type ground-normal wind velocity based on the generalization and modification of the well-used set of equations from  Richards and Hoaxey (1993). This modification has been implemented by Yang et al. (2009) and uses a more mathematically consistent formulation allowing the turbulent kinetic energy to vary with height. Also, using a ~~log-low~~ log-law wind velocity profile and the associated turbulent inflow conditions

145  are considered only to be valid in the atmospheric surface layer, which can be roughly estimated as $10\%$ of the atmospheric boundary layer (Temel et al. 2018). The idealized velocity profile has no wind veer, meaning it does not have a changing wind direction with height.

An alternative to using the idealized profiles is using fully developed profiles obtained from a one-dimensional precursor simulation following the strategies of Koblitz (2013),  Alletto et al.(2018). Cyclic conditions are applied on the sides, and the

150  simulations are run for sufficient iterations to allow development of the profile. The setups are identical to the setups used in the final (successor) simulations except for the computational domain and mesh, the cyclic conditions applied, and the number of iterations. It ~~ensures consistent profiles. The effect of atmospheric stability, a tree canopy, the Coriolis frequency,~~

~~and other parameters are modeled through source terms explained in the following section. It~~ enables the precursor simulations to produce inlet profiles valid for various conditions, including non-neutral atmospheric conditions. Adjusting the parameters of these source terms is an efficient way to obtain the desired inflow. The developed velocity profile has wind veer, meaning the wind turns clockwise with height caused by the balance between friction, the Coriolis force, and the pressure gradient force, and that Perdigao is located in the Northern Hemisphere.

An overview of the boundary conditions (BCs) used is presented in Table 1.

**Table 1.** Overview of boundary conditions applied in the neutral simulation setup.

| Patch | Boundary condition type |
|---|---|
| Sides | Inlet/outlet |
| Inlet | Fixed value profiles of an atmospheric boundary layer |
| Outlet | Zero gradient, and fixed pressure or fixed $(p - (\rho gh))$ |
| Terrain | Rough wall, $z_0 = 0.02\,\mathrm{m}$ |
| Top | Slip |

Robin boundary conditions that act as an inlet or outlet are used on the sides of the domain to simulate wind from any horizontal direction. The direction of the flux automatically determines the inlet and outlet regions. The inlet profiles are fixed to form a homogeneous atmospheric boundary layer (ABL), either idealized profiles representing neutral atmospheric conditions or fully developed profiles obtained from precursor simulation based on the work of (van der Laan et al., 2020). ~~At the outlet, outlet~~ Outlet conditions were used with constant pressure in the simulations using the SF solver, or equally, constant $(p - (\rho gh))$ in the simulations using the BBSF solver. Zero gradient was set for the remaining variables. The direction of the flux automatically determines the inlet and outlet regions. No-slip conditions with wall functions were used for the terrain. Specifically, a rough wall condition was applied ~~( (~~ Hargreaves and Wright, 2007). The roughness was set to $z_0 = 0.02\,\mathrm{m}$, based on average values of a roughness map provided at the database of the Perdigão field experiment (Fernando et al., 2018).

### 3.2 Source terms

~~Four~~ Three different source terms have been added to the momentum equation for some of the simulation cases: Tree canopy as a porous medium, Coriolis force, ~~Pressure gradient force, Buoyancy forces, maximum mixing length scale limiter for the mixing length turbulence model.~~ and pressure gradient force. Additionally, a limiter in the turbulence dissipation equation was added to one of the cases.

~~Some simulation cases include the modeling of a tree canopy through a source term.~~

The canopy is modeled as a porous medium based on the work of ~~Costa (~~ Costa (2007). A drag term is added to the momentum equation ~~and additional source terms for the production and dissipation of turbulence. The porous media is implemented through~~ . The canopy source term was utilized with the `simpleFoam` (SF) flow solver. The porosity model is based on the `powerLawLopesdaCosta` model implemented in OpenFOAM. It is a variant of the power law porosity model ~~. The parameters for the canopy modeling are~~ with spatially varying drag coefficient. This source term is applied to the momentum

equation to reproduce the momentum dissipation that the trees and its foliage should produce in the flow. The following parameters are used: Porosity surface area per unit volume or the leaf area density ($\Sigma = 1.0$), Drag coefficient ($C_d = 0.25$), ~~which is set to $0.14\,\mathrm{m}^{-1}$,~~ and the ~~drag coefficient of the trees, set to $0.25$~~ Power law model exponent coefficient ($C1 = 2.0$) for the Equation 2. A mean tree height of $3\,\mathrm{m}$ is chosen based on the mean canopy height at different locations provided by Vasil-jevic et al. (2017). This was applied all over the entire flow domain. A cell set was utilized to select a volume of cells 3 m above the ground (this forms a canopy zone where the source terms are activated). An overall tree height of $3\,\mathrm{m}$ is also supported by analyzing a LiDAR point cloud acquired from the database of the Perdigão field experiment (Fernando et al., 2018) as shown in Fig. 5. The source term in the canopy model for velocity is as shown below:

$$S_p - = \alpha \rho \left( C_d \underline{LAD}\Sigma \, |u_o| \right) u \tag{2}$$

where ~~$LAD$~~ $\Sigma$ is the Leaf area density, $C_d$ is the plant canopy drag coefficient. As highlighted in Lalic and Mihailovic (**?**), forests have a higher foliage density at the half top than at the bottom zones. However, for the present case, simulations are performed with a uniform leaf area density.

$d$ (m)
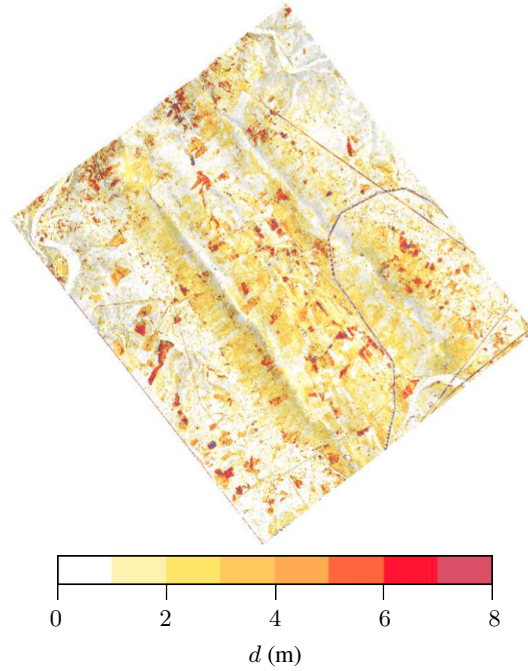
**Figure 5.** Minimum Euclidean distance, $d$, from the trees/vegetation to the bare ground effectively showing their height. Results obtained from analyzing a LiDAR point cloud acquired from the database of the Perdigao Field Experiment website *https://perdigao.fe.up.pt/*.

The ~~magnitude and direction of the~~ Coriolis force source term is included as a momentum source term ($U$ and $V$ momentum equations). The Coriolis force is calculated based on ~~Earths' rotation and the Coriolis frequency parameter corresponding to~~

the latitudeof Perdigão shown in Eq. ??.

$$f_M - = \rho((2\Omega) \times u)$$

where $\Omega$ is the rotational period and $\rho$ is the air densitythe planetary rotational period ($\Omega = 24\,h$) and the latitude ($\lambda$) for Perdigao (39.68 °N), where $f_c = 2\Omega sin(\lambda)$. Similar to Koblitz 2013, the Coriolis force in vertical direction is neglected since it is negligible compared to the gravitational acceleration.

A pressure gradient force forcing term is also included in the simulation cases using the BBSF solver. In setups using this solver, the wind is driven by the balance of the lateral pressure gradient force and the Coriolis force, which are added in the momentum equation as shown in equations provided in the Appendix . This balance is called geostrophic balance, and the resulting wind is a geostrophic wind, which in the Northern Hemisphere goes counterclockwise around low-pressure systems.

The inclusion of buoyancy forces is enabled by adding a heat/cooling flux on the terrain patch and adjusting the maximum mixing length scale, $L_{max}$, through the use of the source terms for turbulent kinetic energy and dissipation shown in Eqn. ??. These buoyancy forces are required in modeling non-neutral atmospheric effects and are only possible using the BBSF solver of the two solvers used .

$$B = \beta_B \alpha_{t_o}(\nabla T_o \cdot \boldsymbol{g}), \quad S_p = \rho \frac{B}{k_o} k, \quad S_p = \rho \frac{C_3 B}{k_o} \epsilon$$

where $B$ is the buoyancy production term, $\beta_B$ is the thermal expansion coefficient, $\alpha_{t_o}$ is the kinematic turbulent thermal conductivity, $k$ is the turbulent kinetic energy, $\epsilon$ is the turbulent kinetic energy dissipation rate, $C_3$ is a model constant. Terms with the subscript denote values for previous iteration.

The level of turbulent kinetic energy is controlled in the domain by the use of a parameter called the maximum turbulent mixing length scale, used is to limit the production and dissipation terms of the turbulence model. The maximum global turbulent mixing length scale for a neutral ABL as is shown in Eq. 3 proposed by (Blackadar, 1962) Blackadar (1962) and also used by (Koblitz, 2013). Koblitz (2013). Ambient source terms were added to avoid zero turbulence values above the ABL similar to mentioned in (?) and applied to the entire domain. The values were set to $k_{Amb} = 0.001$ and $\epsilon_{Amb} = 7.208e - 08$ as summarized in Table 3.

$$L_o = 0.00027 \frac{G}{f_c} \tag{3}$$

where G is the geostrophic wind and $f_c$ is the Coriolis frequency parameter.

The governing equations for the BBSF solver and the different source terms are further detailed in the Appendix .

### 3.3 Simulation cases

The setup for all the simulations was identical except for certain parameters. The solver used is either `simpleFoam` (SF) or `buoyantBoussinesqSimpleFoam` (BBSF). The inlet profiles, either idealized with a logarithmic velocity profile representing neutral atmospheric conditions or fully developed profiles obtained from precursor simulation. Source terms added,

including canopy (tree height set to $3\,\text{m}$) and the Coriolis force. Three turbulence models have been used: the standard k-$\epsilon$ turbulence model (SKE), a modified k-$\epsilon$ turbulence model (MKE), and the k-$\omega$ turbulence model (KO). The MKE model is applied in the simulation case where trees/vegetation (canopy) has been added as a porous medium with the SF solver. The turbulent constans are modified with $C_\mu = 0.033$. This model was tuned using experimental data and LES (Large Eddy Simulation) for a homogeneous forest (Costa 2007). With regards to the boundary conditions, they are overall the same but had to be adjusted to account for the different solvers and inlet profiles used. An overview of all the simulation cases is provided in Table 2. The set of chosen turbulence constants are shown in Table 3.

**Table 2.** List of simulation cases simulating a period of neutral atmosphere, 22:00-22:30 (04.05.17).

| Case name | Solver | Inlet profiles | Source terms | | | Turbulence mod. |
|---|---|---|---|---|---|---|
| | | | Canopy | Coriolis | Pres. gr. | |
| SF1 | SF | Idealized | No | No | No | SKE |
| SF2 | SF | Idealized | No | No | No | KO |
| SF3 | SF | Idealized | Yes | No | No | MKE |
| SF4 | SF | Idealized | No | Yes | No | SKE |
| BBSF1 | BBSF | Precursor | No | Yes | Yes | KE-Lim |

Numerical convergence difficulties can be encountered when using the global turbulence length scale limiter (?) when applied to the present case for simulations over the complex terrain of Perdigao. This is especially true when setting the values of the maximum limiting length scale to low values. Here, the model is trying to restrict the turbulence scale, but physically the large length scales of turbulence are produced from hills or features that are are in the order of the maximum value that is set by turbulence model.

## 4 Results

The results are discussed based on three groups of towers of interest: on top of the ~~South-West~~ Southwest ridge, inside the valley and on top of the ~~North-East~~ Northeast ridge. The inlet profiles for all the simulations are calibrated to match the measured velocity magnitude and direction at 100 m at tower 20, which corresponds to an elevation of 573 m. Different metrics are analyzed for all the simulation models at different towers and are further explained. The root mean square error (RMSE) between the averaged profiles of the measured data and the simulated results is computed and presented in Table 4. A hit rate metric for a given model is defined as the number of predictions ~~predictions~~ within one standard deviation over each height of the field measurement. The relative error for the turbulent kinetic energy and wind direction is shown in Tables 5, 6 respectively. The relative error is defined as the percentage of difference between the simulated and field measurement, which is divided by field measurement value. The error bars represent the standard deviation of the mean measurements.

**Table 3.** Turbulence constants for different turbulence models

| Coefficient | Turbulence model | | | |
|---|---|---|---|---|
| | SKE | MKE | KO | KE-Lim |
| $C_\mu$ | 0.09 | 0.033 | 0.09 | 0.09 |
| C1 | 1.44 | 1.44 | - | 1.44 |
| C2 | 1.92 | 1.92 | - | 1.92 |
| $\sigma_\epsilon$ | 1.30 | 1.85 | - | 1.30 |
| $\sigma_K$ | 1.0 | - | 0.5 | - |
| $\alpha_K$ | - | | 0.5 | - |
| $\alpha_\omega$ | - | - | 0.6 | - |
| $\beta*$ | 0.09 | - | - | 0.09 |
| $\beta$ | - | - | 0.072 | - |
| $\nu$ | 1.5e-05 | 1.5e-05 | 1.5e-05 | 1.5e-05 |
| $L_{max}$ | - | - | - | 62.14 |
| $k_{Amb}$ | - | - | - | 0.001 |
| $\epsilon_{Amb}$ | - | - | - | $7.208e-08$ |
| $T_{Ref}$ | - | - | - | 300 |
| $Pr$ | - | - | - | 0.9 |
| $Prt$ | - | - | - | 0.74 |

## 4.1 Model prediction on SW ridge

The towers on the SW ridge as shown in Fig. 2 are the Tower 20, 34 and 37. This is a region of flow acceleration. ~~A good match is obtained in between the measured and computed velocity , turbulent kinetic energy and wind direction profiles for the calibration~~ The inflow profile is calibrated to match the velocity at 100 m height for Tower 20 as ~~seen in~~ shown in the wind velocity profiles shown in Fig. ~~??. For Tower~~ 6 (a) at 100 m. All models except the canopy model (SF3) shows an over prediction of the velocity profiles close to the ground at Tower 20. The canopy model (SF3) underpredicts the velocity close to the ground but correctly predicts the decrease in velocity close to the ground. This prediction could be improved by considering a non uniform tree height and removing the canopy source terms on top of the ridges. On the other hand, at Tower 34 shown in Fig ~~?? and for~~ 6 (b), the canopy model (SF3) shows a good match with the field measurement, and on Tower 37 ~~shown seen~~ in Fig ~~??, the model including the canopy provides the best match~~ 6 (c), shows a slight under prediction. In models that do not account for a canopy (SF1, SF2, ~~a speed up~~ SF4 and BBSF1), a speed-up is seen close to the ground with large RMSE errors as ~~seen~~ shown in Table 4. The ~~canopy model on the other hand predicts the shape of the profile correctly, but over predicts the turbulent kinetic energy for all the towers on the SW ridge. The~~ results suggest that the inclusion of the canopy is a good choice for prediction of velocity profiles, however the ~~parameter choice needs to be better optimised to reduce the levels of turbulence produced due by the canopy.~~ canopy parameters need to be adapted based on the forest point cloud data. The

**Table 4.** RMSE for wind speed predictions on the main towers of interest.

| Case | Weather mast and group | RMSE (m/s) Height over terrain | | | | | | | Average RMSE (m/s) | Hit rate (max 7) |
|---|---|---|---|---|---|---|---|---|---|---|
| | | 10 m | 20 m | 30 m | 40 m | 60 m | 80 m | 100 m | | |
| SF1 (k-$\epsilon$) | Tower 20 (SW rid.) | 0.82 | 0.29 | 0.25 | 0.22 | 0.30 | 0.21 | 0.23 | 0.33 | 6 |
| | Tower 25 (valley) | 0.90 | 1.05 | 1.02 | 0.84 | 0.73 | 0.59 | 0.57 | 0.81 | 3 |
| | Tower 29 (NE rid.) | 1.53 | 0.73 | 0.46 | 0.15 | 0.44 | 0.41 | 0.43 | 0.59 | 6 |
| SF2 (k-$\omega$) | Tower 20 (SW rid.) | 0.78 | 0.23 | 0.20 | 0.17 | 0.26 | 0.17 | 0.19 | 0.29 | 6 |
| | Tower 25 (valley) | 0.19 | 0.65 | 0.74 | 0.69 | 0.75 | 0.69 | 0.71 | 0.63 | 0 |
| | Tower 29 (NE rid.) | 0.66 | 0.96 | 1.19 | 1.19 | 1.37 | 1.28 | 1.23 | 1.12 | 1 |
| SF3 (canopy) | Tower 20 (SW rid.) | 0.66 | 0.51 | 0.42 | 0.34 | 0.38 | 0.26 | 0.19 | 0.39 | 2 |
| | Tower 25 (valley) | 0.18 | 0.39 | 0.42 | 0.45 | 0.63 | 0.84 | 1.02 | 0.56 | 0 |
| | Tower 29 (NE rid.) | 2.40 | 3.03 | 3.20 | 3.16 | 3.17 | 2.99 | 2.81 | 2.97 | 0 |
| SF4 (Coriolis) | Tower 20 (SW rid.) | 0.41 | 0.57 | 0.59 | 0.62 | 0.88 | 0.82 | 0.85 | 0.68 | 7 |
| | Tower 25 (valley) | 1.52 | 1.84 | 1.84 | 1.69 | 1.52 | 1.24 | 1.11 | 1.54 | 3 |
| | Tower 29 (NE rid.) | 0.65 | 1.47 | 1.76 | 1.88 | 2.08 | 1.87 | 1.75 | 1.64 | 0 |
| BBSF1 (k-$\epsilon$ Lim) | Tower 20 (SW rid.) | 1.02 | 0.42 | 0.38 | 0.33 | 0.08 | 0.09 | 0.09 | 0.34 | 6 |
| | Tower 25 (valley) | 1.52 | 1.73 | 1.81 | 1.79 | 1.94 | 2.13 | 2.28 | 1.89 | 0 |
| | Tower 29 (NE rid.) | 2.08 | 1.26 | 0.95 | 0.70 | 0.39 | 0.42 | 0.48 | 0.89 | 5 |

turbulent kinetic energy profiles are shown in Fig 7, showing a good prediction for all the models except the Canopy model (S3) which produces excessive turbulence levels compared to field measurements. BBSF1 model (k-$\epsilon$ Lim) shows a good match to the field measurement at Towers 20 and 34. Fig 8 shows the predicted wind direction profiles at the three towers. The BBSF1 model (k-$\epsilon$ Lim) shows the best prediction for the wind direction overall as seen in Table 6. As highlighted in the methodology section, there is a large uncertainty in wind direction seen in the field experiment that varies with location and height, and for a complex terrain a small change inflow direction could play an important role in the predicted wind direction profiles at the mast. This highlights a limitation in the models' ability to represent actual conditions for such a complex site. SF4 model (Coriolis) shows a large wind veer that affects the wind direction prediction, which indicates that this needs to be tuned in the inflow profile for this model to account for this flow turning. In terms of the turbulence model, the $k - \epsilon$ model SF1 model (k-$\epsilon$) is seen to produce a slightly greater speed up compared to the $k - \omega$ model SF2 model (k-$\omega$), but overall the prediction capability for the wind speed, turbulent kinetic energy and wind speed is similar.

## 4.2 Model prediction inside the valley

The towers of interest inside the valley are Towers 25, 227, 27 and 7. The predicted velocity, turbulent kinetic energy and wind direction 22 as seen earlier in Fig 2. The valley is a region of strong flow separation and flow re-circulation. The predicted velocity profiles are shown in Figs **??, ?? and ??** respectively. This is a region of strong flow separation and flow

**Table 5.** Relative error and hit rate metrics for turbulent kinetic energy predictions at the main towers of interest.

| Case | Weather mast and group | Average relative difference in TKE (%) | Hit rate (max 7) |
|---|---|---|---|
| SF1 (k-$\epsilon$) | Tower 20 (SW rid.) | 11.27 | 7 |
| | Tower 25 (valley) | 55.43 | 6 |
| | Tower 29 (NE rid.) | 46.02 | 4 |
| SF2 (k-$\omega$) | Tower 20 (SW rid.) | 9.93 | 7 |
| | Tower 25 (valley) | 59.20 | 4 |
| | Tower 29 (NE rid.) | 24.26 | 5 |
| SF3 (canopy) | Tower 20 (SW rid.) | 105.65 | 0 |
| | Tower 25 (valley) | 61.40 | 3 |
| | Tower 29 (NE rid.) | 34.26 | 4 |
| SF4 (Coriolis) | Tower 20 (SW rid.) | 10.65 | 7 |
| | Tower 25 (valley) | 55.77 | 6 |
| | Tower 29 (NE rid.) | 42.52 | 3 |
| BBSF1 (k-$\epsilon$ Lim) | Tower 20 (SW rid.) | 16.80 | 7 |
| | Tower 25 (valley) | 35.71 | 7 |
| | Tower 29 (NE rid.) | 57.66 | 0 |

**Table 6.** Relative error and hit rate metrics for wind direction predictions at the main towers of interest.

| Case | Weather mast and group | Average difference in wind direction ($°$) | Hit rate (max 7) |
|---|---|---|---|
| SF1 (k-$\epsilon$) | Tower 20 (SW rid.) | 1.99 | 6 |
| | Tower 25 (valley) | 36.59 | 4 |
| | Tower 29 (NE rid.) | 4.18 | 7 |
| SF2 (k-$\omega$) | Tower 20 (SW rid.) | 1.84 | 6 |
| | Tower 25 (valley) | 53.23 | 2 |
| | Tower 29 (NE rid.) | 4.22 | 7 |
| SF3 (canopy) | Tower 20 (SW rid.) | 1.82 | 6 |
| | Tower 25 (valley) | 74.43 | 0 |
| | Tower 29 (NE rid.) | 7.00 | 4 |
| SF4 (Coriolis) | Tower 20 (SW rid.) | 6.25 | 6 |
| | Tower 25 (valley) | 135.81 | 2 |
| | Tower 29 (NE rid.) | 11.82 | 1 |
| BBSF1 (k-$\epsilon$ Lim) | Tower 20 (SW rid.) | 2.39 | 6 |
| | Tower 25 (valley) | 28.26 | 7 |
| | Tower 29 (NE rid.) | 5.34 | 7 |
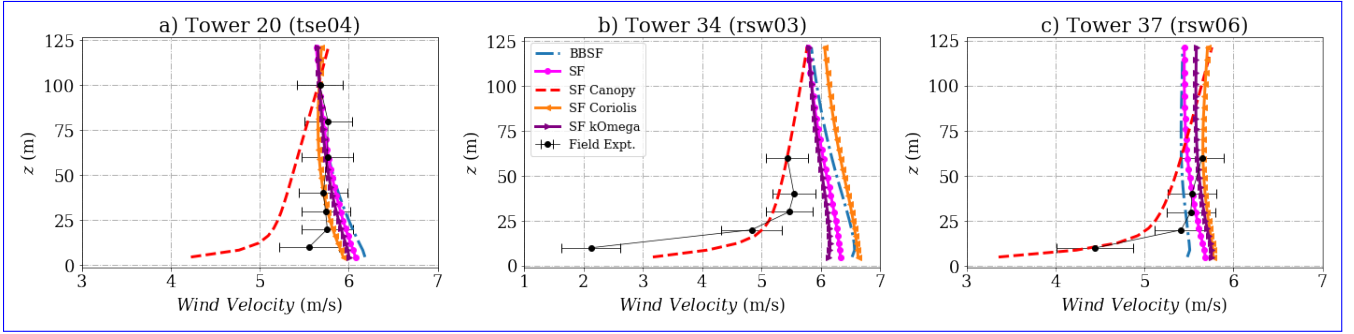
**Figure 6.** Simulation results and experimental data ~~in tower 20/ tse04~~ for ~~SW winds: (~~wind velocity on the Southwest ridge for a) ~~wind speed,~~ Tower 20 (tse04) b) ~~turbulent kinetic energy~~ Tower 34 (rsw03) c) ~~wind direction~~Tower 37 (rsw06). The locations of the masts are given in Fig 2.
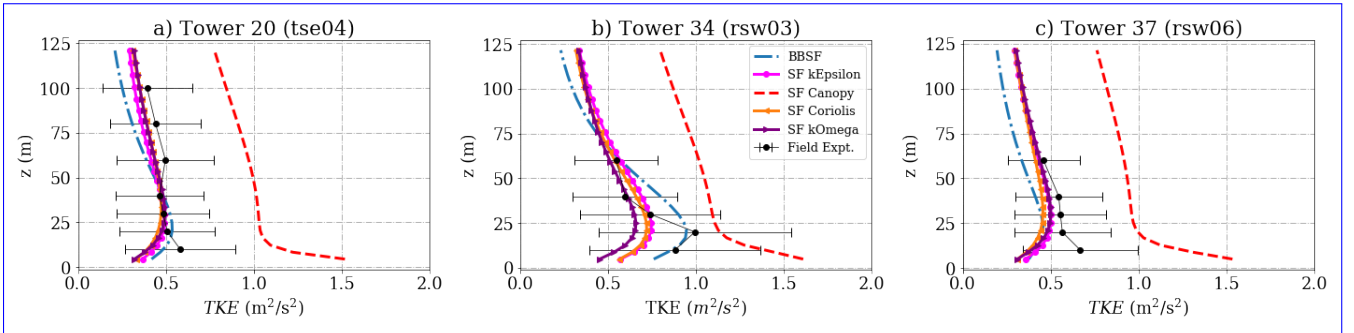
**Figure 7.** Simulation results and experimental data ~~in tower 34/ rsw03~~ for ~~SW winds: (~~turbulent kinetic energy on the Southwest ridge for a) ~~wind speed,~~ Tower 20 (tse04) b) ~~turbulent kinetic energy~~ Tower 34 (rsw03) c) ~~wind direction~~Tower 37 (rsw06). The locations of the masts are given in Fig 2.
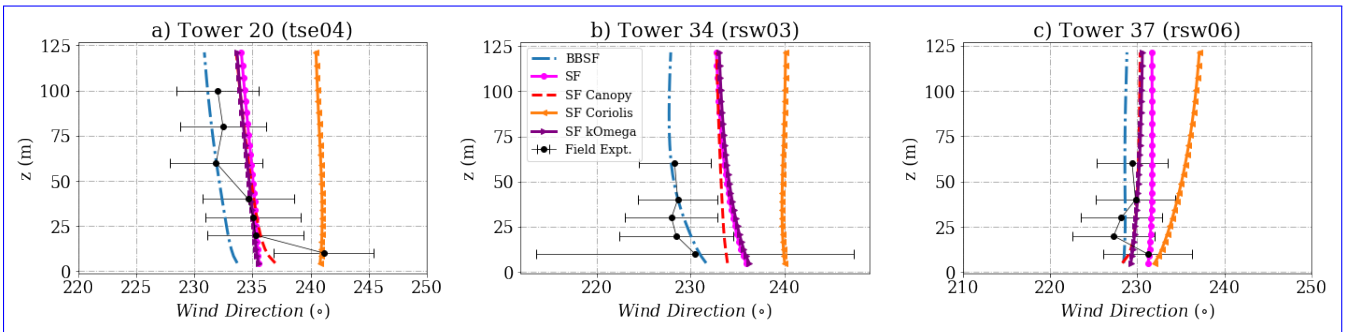
**Figure 8.** Simulation results and experimental data ~~in tower 37/ rsw06~~ for ~~SW winds: (~~wind direction on the Southwest ridge for a) ~~wind speed,~~ Tower 20 (tse04) b) ~~turbulent kinetic energy~~ Tower 34 (rsw03) c) ~~wind direction~~Tower 37 (rsw06). The locations of the masts are given in Fig 2.

re-circulation. 9 and 10. At Towers 25, 22 and 27 the canopy model significantly underpredicts the velocity profiles. On the other hand, the canopy model shows the best prediction at Tower 7, which is located the lowest in altitude among the other towers. The BBSF1 model overestimates the velocity at Tower 25 and all models show an under prediction at Tower 22. The SF1 $(k-\epsilon)$ model performs better than the SF2 $(k-\omega)$ model in prediction of wind velocity.
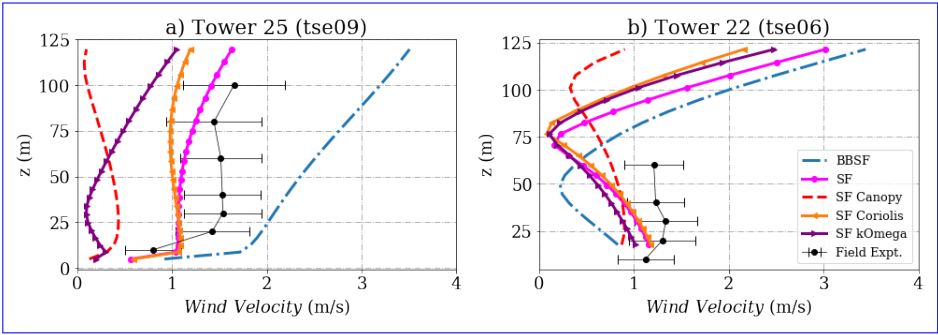
**Figure 9.** Simulation results and experimental data wind velocity inside the valley for a) Tower 25 (tse09) b) Tower 22 (tse06). The locations of the masts are given in Fig. 2.
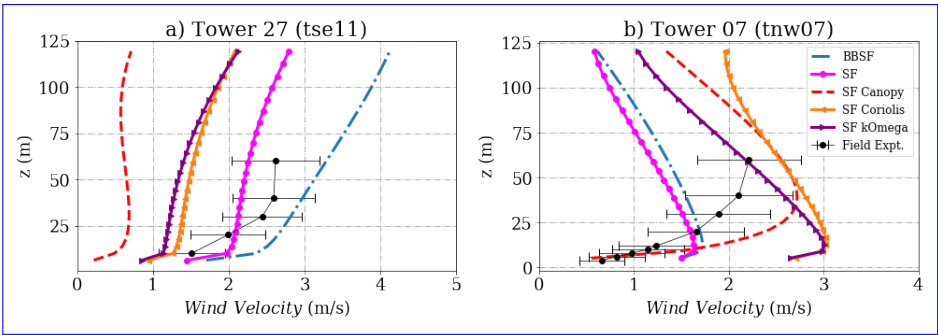
**Figure 10.** Simulation results and experimental data for wind velocity inside the valley for a) Tower 27 (tse11) b) Tower 7 (tnw07). The locations of the masts are given in Fig. 2.

280    Figs. 11 and 12 show a comparison of turbulent kinetic energy profiles between the present model predictions and the field measurements. The measured values of turbulent kinetic energy is are high inside the valley at all met-mast locations, indicative of flow mixing and high turbulence, however all the models seem to strongly under predict underpredict the turbulent kinetic energy with large relative errors as seen in Table 5, except for Tower 22 which is located the closest to the South-West ridge. Almost all models seen to provide a good prediction of the velocity profiles and TKE at that location, however a Southwest
285   ridge.

    The wind direction profiles are shown in Figs. 13 and 14 respectively. A sudden shift in wind direction, indicative of a flow separation and re-circulation is seen in Fig ??. The buoyancy model . 13. The BBSF1 model (k-$\epsilon$ Lim) provides a good hit rate
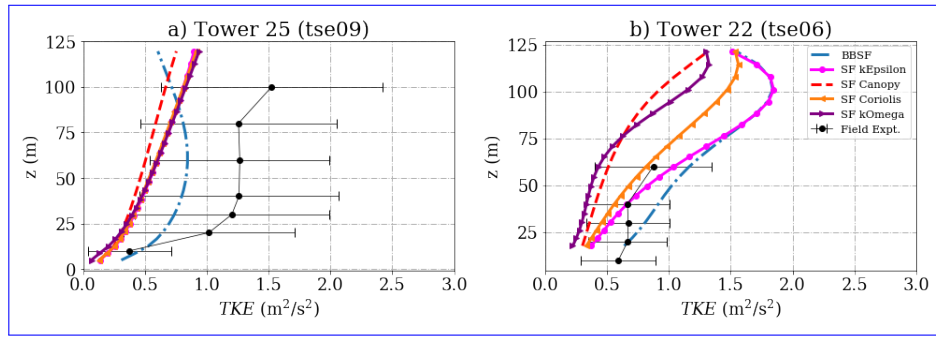
**Figure 11.** Simulation results and experimental data for turbulent kinetic energy inside the valley for a) Tower 25 (tse09) b) Tower 22 (tse06). The locations of the masts are given in Fig. 2.
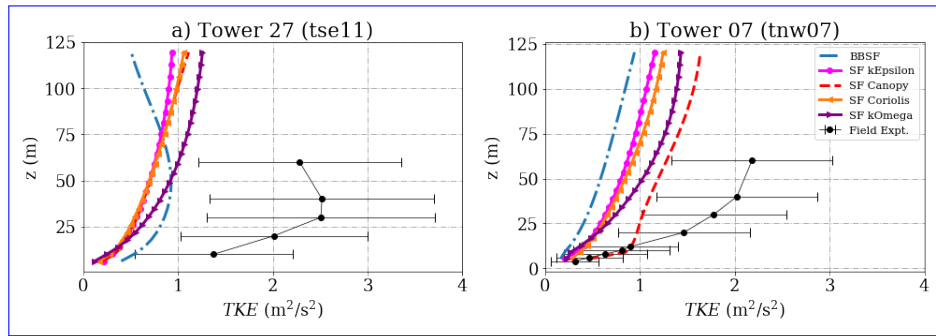
**Figure 12.** Simulation results and experimental data for turbulent kinetic energy inside the valley for a) Tower 27 (tse11) b) Tower 7 (tnw07). The locations of the masts are given in Fig. 2.

for the wind direction inside the valley as shown in Table 6. ~~On comparison of the turbulence the turbulence model, the $k - \epsilon$ model performs better than the $k - \omega$ model in prediction of wind velocity.~~ Fig. 15 shows the velocity contour for the predicted

290 re-circulation zone inside the valley ~~using the canopy and buoyancy models. The model with the canopyproduces a larger~~ for the SF3 model (canopy) and the BBSF1 model (k-$\epsilon$ Lim). The SF3 model (canopy) produces a single large re-circulation zone compared to the other models~~.~~, and a smaller and double re-circulation zone seen for the BBSF1 model (k-$\epsilon$ Lim). This is seen as a large under prediction of the velocity profiles seen earlier in Figs. 9 and 10 for the canopy model.

~~Simulation results and experimental data in tower 25/ tse09 for SW winds: (a) wind speed, (b) turbulent kinetic energy (c)~~
295 ~~wind direction~~

**Figure 13.** Simulation results and experimental data ~~in tower 7/ tnw07~~ for ~~SW winds: (~~wind direction inside the valley for a) ~~wind speed,~~ Tower 25 (tse09) b) ~~turbulent kinetic energy~~ Tower 22 (~~e~~tse06)~~wind direction~~. The locations of the masts are given in Fig. 2.

~~Simulation results and experimental data in tower 27/ tse11 for SW winds: (a) wind speed, (b) turbulent kinetic energy (c) wind direction~~
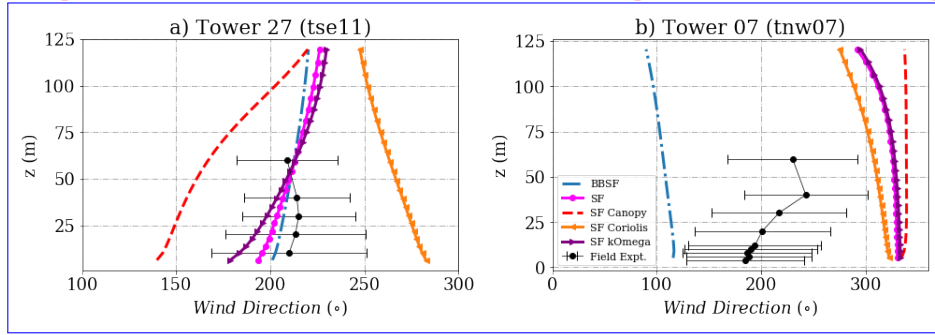
**Figure 14.** Simulation results and experimental data ~~in tower 22/ tse06~~ for ~~SW winds: (~~wind direction inside the valley for a) ~~wind speed,~~ Tower 27 (tse11) b) ~~turbulent kinetic energy~~ Tower 7 (~~e~~tnw07)~~wind direction~~. The locations of the masts are given in Fig. 2.

### 4.3  Tower Prediction on NE ridge

The ~~predictions for towers on the North-East ridge~~ wind velocity profiles for Tower 29 and Tower 10 on the Northeast ridge are shown in ~~Figs. ?? and ??~~Fig. 16. This is a region of flow acceleration on top of the ridge downstream from re-circulation zone inside the valley, which makes the predictions quite challenging. The ~~canopy model~~ SF3 model (canopy) is seen to under predict significantly the velocity profiles on top of this ridge. Both the baseline SF1 ($k - \epsilon$ ~~model and buyoantBoussinesqSimpleFoam model~~) model and the BBSF1 model (k-$\epsilon$ Lim) appears to provide a good prediction of the velocity profile and wind direction for the Tower ~~29 and also Tower 10 upto 40 m.~~ 29. The region near ~~tower~~ Tower 10 comprises of a mountain gap~~(~~ (Vassallo et al. 2020), which could indicate that a higher terrain resolution is required surrounding this region to improve the prediction accuracy. Excessive levels of turbulence is seen close to the ground in the field measurements shown in Fig. 17. All models appear to underpredict the field measurements close to the ground and the SF3 (canopy) shows the closest match. The BBSF1 model (k-$\epsilon$ Lim) underpredicts the turbulence levels, due to the use of the maximum length scale limiter. The wind direction profiles at the towers are shown in Fig. 18. As seen for the TKE profiles, a large uncertainty is seen in the wind direction on
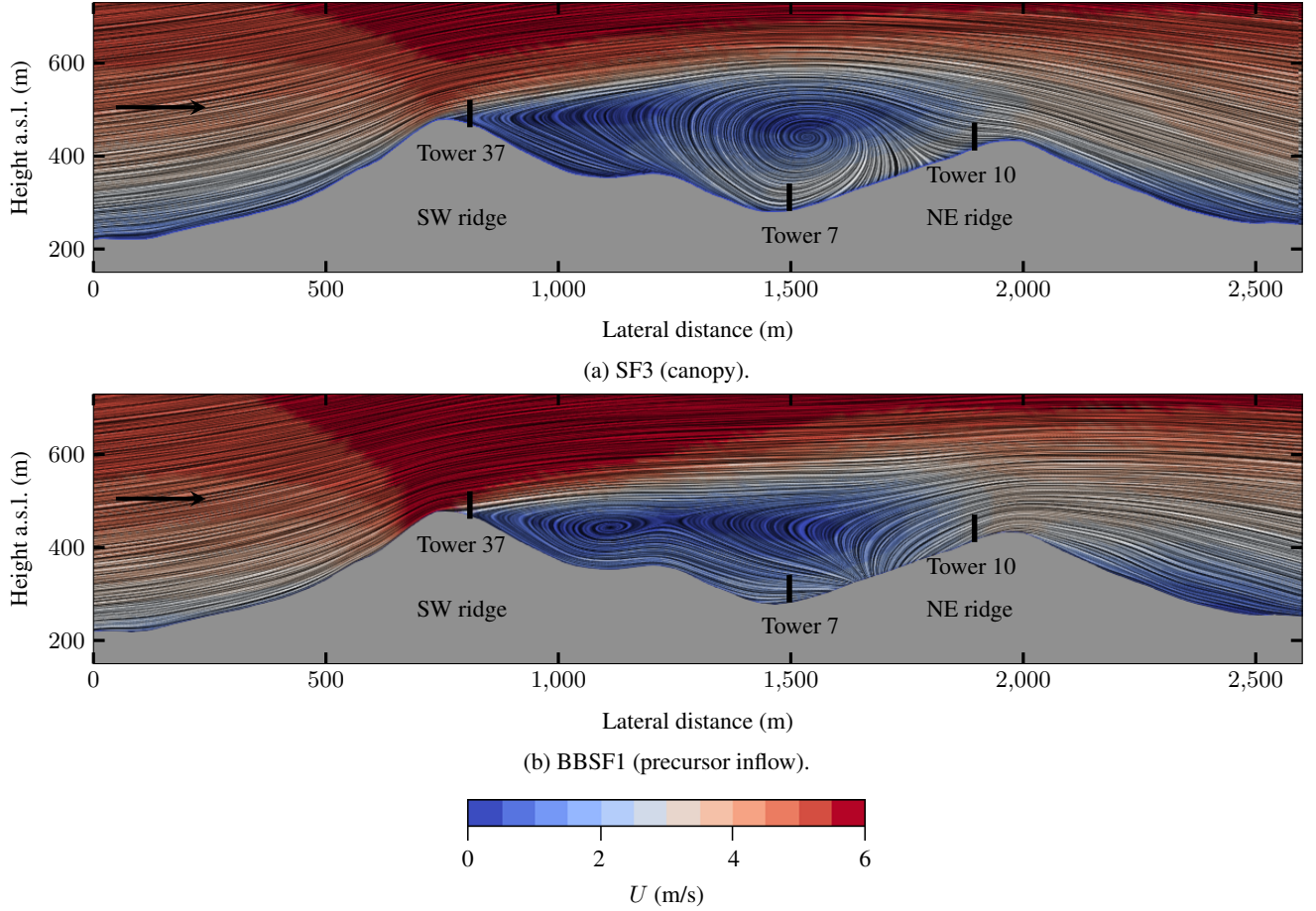
**Figure 15.** Vertical slice illustrating the re-circulation zones inside the valley. Flow patterns and velocity magnitude, $U$, are visualized through the technique line integral convolution (LIC). The black lines represent the location and height of the nearest measurement towers in front of or behind the slice. The black arrows indicate the wind direction at the inlet, wind from SW at $231°$, which is parallel to the orientation of the presented slice. The slice location and the locations of the masts are given in Fig. 2.

310
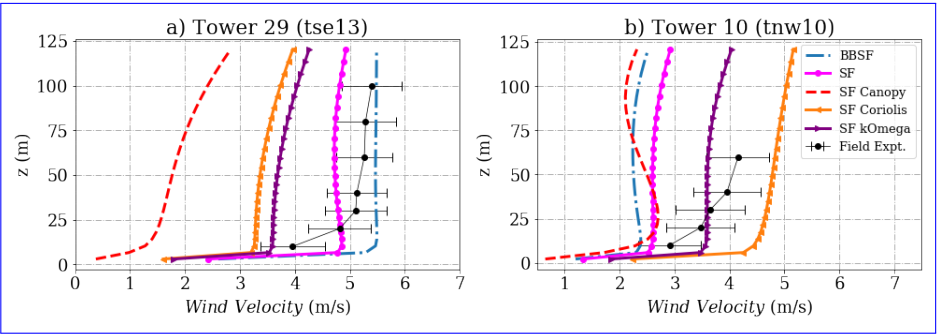
**Figure 16.** Simulation results and experimental data ~~in tower 29/ tse13~~ for ~~SW winds: (~~wind velocity on the Northeast ridge for a) ~~wind speed,~~ Tower 29 (tse13) b) ~~turbulent kinetic energy~~ Tower 10 (~~e~~tnw10)~~wind direction~~. The locations of the masts are given in Fig. 2.
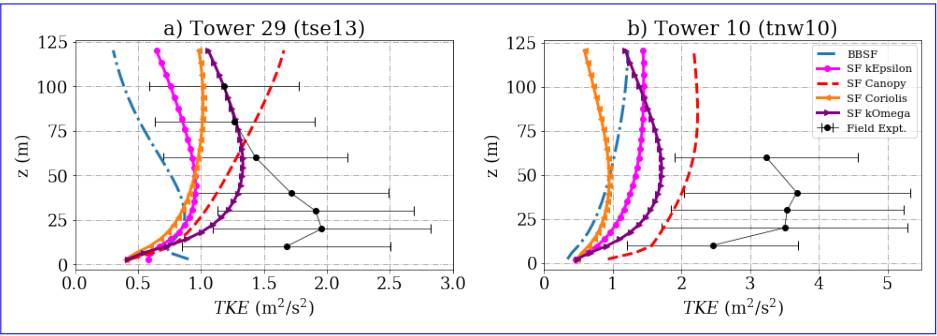
**Figure 17.** Simulation results and experimental data ~~in tower 10/ tnw10~~ for ~~SW winds: (~~turbulent kinetic energy on the Northeast ridge for a) ~~wind speed,~~ Tower 29 (tse13) b) ~~turbulent kinetic energy~~ Tower 10 (~~e~~tnw10)~~wind direction~~. The locations of the masts are given in Fig. 2.

## 5 Conclusions

A Reynolds-averaged Navier-Stokes (RANS) model is setup using OpenFOAM (version 2012) to simulate a ~~30 min averaged~~ 30-min averaged stationary period corresponding to ~~a neutral atmospheric stability condition at Tower 20.~~ near-neutral conditions at met-mast Tower 20 located at the Southwest ridge. In that period and for that tower, the wind is coming from Southwest

315 at 231° at 100 m height above ground. Five different models are simulated comprising of different source terms to take into account the effects of canopy, the Coriolis force and pressure gradient force, and two different inflow profiles. One idealized set with a log-law velocity profile, and one set of fully developed profiles based on a precursor simulation. The predicted profiles are analysed in terms of the different groups of towers on top of the ridges and inside the valley based on the flow topology.
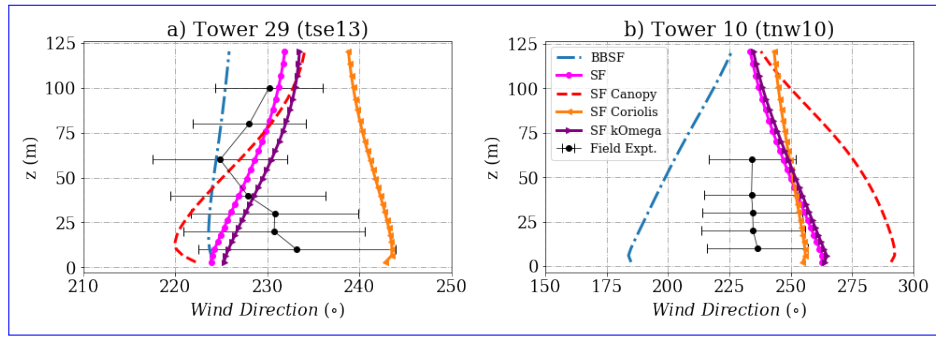
**Figure 18.** Simulation results and experimental data for wind direction on the Northeast ridge for a) Tower 29 (tse13) b) Tower 10 (tnw10). The locations of the masts are given in Fig. 2.

~~Five different models are simulated comprising of different source terms to take into account the effects of buoyancy, canopy,~~
320 ~~Coriolis forces.~~ The complex terrain site of Perdigão represents a large spatial variability of forest canopy and surface elevation, which contribute to variable ~~thermal stability~~ flow topology at different met-masts. The key conclusions for different groups of towers are summarised as follows:

a) **For the towers on the ~~South-West~~ Southwest ridge:** The region at the ~~South-West~~ Southwest ridge is a zone ~~flow~~
325 ~~acceleration upstream of the inflow wind direction.~~ of flow acceleration at the first oncoming ridge downstream of the inlet for wind coming from the Southwest. The inflow profiles are calibrated to closely match the wind speed and wind direction at Tower 20. The use of ~~canopy model~~ a canopy model (SF3) decreases the velocities near the surface and a closer match with field data ~~. Other models over-predict~~ at Tower 34 and 37. Other models overpredict the velocity profile close to the ground. However, the canopy parameters need to be tuned as the surface heterogeneity is not taken into account as the prediction accu-
330 racy varies at the different locations along the ridge.

b) **For the towers inside the valley:** The valley is a zone of flow re-circulation ~~.~~ and comprises lower velocities and higher variability which remains challenging for prediction models. ~~The BBSF model is shown to provide~~ Moreover, large uncertainties are seen in the wind velocity, wind direction and turbulent kinetic energy profiles for the field measurements. The
335 prediction capabilities of the models vary with the tower location inside the valley. At Tower 25 and 27, the SF1 model (k-$\epsilon$) provides the best prediction for wind velocity. The BBSF1 model (k-$\epsilon$ Lim) provides the best prediction of wind direction. Large relative errors in wind speed and turbulent kinetic energy profiles are seen for most of the models, especially close to the ground.

340 c) **For the towers on the ~~North-East~~ Northeast ridge**: The region at the ~~North-East~~ Northeast ridge is a zone of flow acceleration downstream of the re-circulation zone from the valley. The precursor inflow model (BBSF1) provides a good prediction on Tower 29 for the wind speed while the canopy model (SF3) provides a strong under-prediction. The prediction

of the extent of the re-circulation inside of the valley and the re-attachment location plays a key role in the prediction profiles on the Northeast ridge. Significant turbulence is seen close to ground in the field measurements, which is under-predicted by

345 most of the models. ~~The model accounting for buoyancy forces provides a good prediction on Tower 29 for the wind speed and direction while the canopy model strongly under predicts the wind speed. Local~~ Finally, local terrain features need to be resolved ~~such as the mountain gap near Tower 10.~~ with a higher resolution such as near Tower 10, which includes a mountain gap.

Finally, the choice of the best turbulence model is found to be inconclusive in terms of overall prediction capability for differ-
350 ent parts of the terrain. In the future, the surface heterogeneity of canopy is to be modelled based on the surface roughness map at Perdigão. ~~The inclusion of the canopy model in buoyantBoussinesq solver could help evaluate the benefit of incorporating both canopy and buoyancy effects together. Furthermore, simulations shall be performedfor periods of non-neutral flow conditions, such as stable or unstable thermal stratification conditions, where the buoyancy effects play an important role.~~ It would be more correct to use different patches with different heights as seen in the forest point cloud data. Simulations using
355 non-uniform leaf area density could also be performed. An important aspect that needs to be assessed is the effect of inflow wind direction uncertainty on the predictions at different tower locations.

*Acknowledgements.* The authors acknowledge the European Commission for its financial support through the project H2020-MSCA-ITN-2019 zEPHYR (Grant Agreement No. 860101). Perdigao data provided by NCAR/EOL under the sponsorship of the National Science Foundation. https://data.eol.ucar.edu/

360 *Author contributions:* KV conceived, coordinated and was responsible for both the work~~and~~, the manuscript writing, and the review process. TOH carried out the numerical simulations, manuscript writing~~and~~, preparation of figures, and attended in the review process. SB helped with conception, manuscript writing and review. KEG helped with model setup and review.

*Competing interests:* The authors declare that they have no conflict of interest.
365 *Data availability:* A community has been setup in Zenodo (https://zenodo.org/communities/zephyr/). A repository of the numerical setup shall be added through Github (https://github.com/kartikv95/WESC-Perdigao).

# References

Alletto, M., Radi, A., Adib, J., Langner, J., Peralta, C., Altmikus, A., and Letzel, M. (2018). E-wind: Steady state cfd approach for stratified flows used for site assessment at enercon. *Journal of Physics: Conference Series*, 1037:072020.

Bechmann, A., Berg, J., Courtney, M., Jørgensen, H., Mann, J., and Sørensen, N. (2009). The bolund experiment: Blind comparison of models for wind in complex terrain (invited). *AGU Fall Meeting Abstracts*.

Blackadar, A. K. (1962). The Vertical Distribution of Wind and Turbulent Exchange in a Neutral Atmosphere. *Journal of Geophysical Research*, 67(3):3095.

Blocken, B. (2014). 50 years of computational wind engineering: Past, present and future. *Journal of Wind Engineering and Industrial Aerodynamics*, 129:69–102.

Brower, M. (2012). Findings of investigations into under-performing sites. In *Proceedings of EWEA Technology Workshop, Lyon, France.* European Wind Energy Association (EWEA).

Carvalho, J. P. D. B. (2019). Analysis of stationary periods during the Perdigao 2017 campaign. Master's thesis, University of Porto, Portugal.

Chavez, R., Rodrigo, J., and Gancarski, P. (2014). Modelling of atmospheric boundary-layer flow in complex terrain with different forest parameterizations. volume 524.

Costa, J. L. C. (2007). Atmospheric flow over forested and non-forested complex terrain.

Desmond, C., Watson, S., and Hancock, P. (2017). Modelling the wind energy resources in complex terrain and atmospheres. numerical simulation and wind tunnel investigation of non-neutral forest canopy flows. *Journal of Wind Engineering and Industrial Aerodynamics*, 166:48–60.

Emeis, S. (2018). *Wind Energy Meteorology*, volume 2 of *Atmospheric Physics for Wind Power Generation*. Springer International Publishing, Belgium.

Fernando, H., Mann, J., Laginha Palma, J., Lundquist, J., Barthelmie, R., Belo-Pereira, M., Brown, W., Chow, F., Gerz, T., Hocut, C., Klein, P., Leo, L., Matos, J., Oncley, S., Pryor, S., Bariteau, L., Bell, T., Bodini, N., Carney, M., and Wang, Y. (2018). The perdigão: Peering into microscale details of mountain winds. *Bulletin of the American Meteorological Society*, 100.

Finnigan, J. (2000). Turbulence in plant canopies. ann rev fluid mech. *Annual Review of Fluid Mechanics*, 32:519–571.

Hågbo, T.-O., Giljarhus, K. E. T., and Hjertager, B. H. (2020). Influence of geometry acquisition method on pedestrian wind simulations. *arXiv preprint arXiv:2010.12371*.

Hargreaves, D. and Wright, N. G. (2007). On the use of the k–$\varepsilon$ model in commercial cfd software to model the neutral atmospheric boundary layer. *Journal of wind engineering and industrial aerodynamics*, 95(5):355–369.

Jørgensen, H., Nielsen, M., Barthelmie, R., and Mortensen, N. (2005). Modelling offshore wind resources and wind conditions. *In Proceedings (CD-ROM) Copenhagen Offshore Wind.*

Kaimal, J. C. and Finnigan, J. J. (1994). *Atmospheric boundary layer flows: Their structure and measurement.* Oxford University Press.

Koblitz, T. (2013). *CFD Modeling of Non-Neutral Atmospheric Boundary Layer Conditions.* PhD thesis, Denmark.

Laginha Palma, J., Silva, C., Costa Gomes, V., Lopes, A., Esteves, T., and Batista, V. (2020). The digital terrain model in the computational modelling of the flow over the perdigão site: the appropriate grid size. *Wind Energy Science*, 5:1469–1485.

OpenFOAM. Openfoam v2012. https://www.openfoam.com/documentation/overview. Accessed: 2021-08-21.

Queck, R., Bienert, A., Maas, H.-G., Harmansa, S., Goldberg, V., and Bernhofer, C. (2012). Wind fields in heterogeneous conifer canopies: Parameterisation of momentum absorption using high-resolution 3d vegetation scans. *European Journal of Forest Research*, 131:165–176.

Richards, P. and Hoaxey, R. (1993). Appropriate boundary conditions for computational wind engineering models using the k-$\epsilon$ turbulence model. In Murakami, S., editor, *Computational Wind Engineering 1*, pages 145–153. Elsevier, Oxford.

Rodrigo, J., Santos, P., Chavez, R., Avila, M., Cavar, D., Lehmkuhl, O., Owen, H., Li, R., and Tromeur, E. (2021). The alex17 diurnal cycles in complex terrain benchmark. *Journal of Physics: Conference Series*, 1934:012002.

Salmon, J., Bowen, A., Hoff, A., Johnson, R., Mickle, R., Taylor, P., Tetzlaff, G., and Walmsley, J. (1988). The askervein hill project: Mean wind variations at fixed heights above ground. *Boundary-Layer Meteorology*, 43:247–271.

Schmidt, J., Peralta, C., and Stoevesandt, B. (2012). Automated generation of structured meshes for wind energy applications. Open Source CFD International Conference, London.

Sogachev, A. (2009). A note on two-equation closure modelling of canopy flow. *Boundary-Layer Meteorology*, 130:423–435.

Sogachev, A. and Panfyorov, O. (2006). Modification of two-equation models to account for plant drag. *Boundary-Layer Meteorology*, 121:229–266.

Sørensen, N. N., Bechmann, A., Réthoré, P.-E., Cavar, D., Kelly, M. C., and Troen, I. (2012). How fine is fine enough when doing CFD terrain simulations. In *EWEA 2012-European Wind Energy Conference & Exhibition*, pages 1167–1172. European Wind Energy Association (EWEA).

Temel, O., Bricteux, L., and Beeck, J. (2018). Coupled wrf-openfoam study of wind flow over complex terrain. *Journal of Wind Engineering and Industrial Aerodynamics*, 174:152–169.

van der Laan, M. P., Kelly, M., Floors, R., and Peña, A. (2020). Rossby number similarity of an atmospheric rans model using limited-length-scale turbulence closures extended to unstable stratification. *Wind Energy Science*, 5:355–374.

Vasiljevic, N., Laginha Palma, J., Angelou, N., Matos, J., Menke, R., Lea, G., Mann, J., Courtney, M., Frölén Ribeiro, L., and Costa Gomes, V. (2017). Perdigão 2015: methodology for atmospheric multi-doppler lidar experiments. *Atmospheric Measurement Techniques Discussions*, pages 1–28.

Vassallo, D., Krishnamurthy, R., Menke, R., and Fernando, H. (2020). Observations of stably stratified flow through a microscale gap. *Journal of the Atmospheric Sciences*, 78.

Wagner, J., Wildmann, N., and Gerz, T. (2019). Improving boundary layer flow simulations over complex terrain by applying a forest parameterization in WRF. *Wind Energ. Sci. Discuss. [preprint]*.

Yang, Y., Gu, M., Chen, S., and Jin, X. (2009). New inflow boundary conditions for modelling the neutral equilibrium atmospheric boundary layer in computational wind engineering. *Journal of Wind Engineering and Industrial Aerodynamics*, 97(2):88–95.

## Grid Independence study

A mesh refinement study has been performed as shown in Table 7, by increasing the number of cells in the x and y direction thereby increasing the horizontal mesh resolution. The case has been simulated using the standard $k - \epsilon$ turbulence model with
435   an idealized set of inlet profiles including a logarithmic velocity profile, and no Coriolis or pressure gradient source term.

**Table 7.** Grid refinement study parameters showing the number of cells per main direction.

| Case | Nx | Ny | Nz | NCells (million) |
|---|---|---|---|---|
| Coarse | 227 | 227 | 120 | 12.7 |
| Medium | 332 | 332 | 120 | 21.19 |
| Fine | 469 | 469 | 120 | 30.6 |

Negligible differences are seen in the velocity and turbulent kinetic energy profiles on top of the ridge at the Tower 20 (Calibration tower) on the South West ridge seen in Fig 19 and at Tower 29 close to 100 m on the North East ridge seen in Fig 20. However, larger differences are seen close to the ground as the topology of terrain is further resolved near the surface upon grid refinement. The structured grids are generated using the `terrainBlockMesher` tool (Schmidt et al., 2012)
440   , which interpolates the SRTM terrain data and creates the terrain patch which on which smoothing is applied towards a cylindrical domain on the sides. Increasing the number of cells refines and slightly modifies the surface mesh close to the ground. Similar differences are seen when using different terrain databases in the grid refinement study by (Laginha Palma et al., 2020) . Furthermore, a small change in the prediction of extent of the re-circulation zone could have a significant change and uncertainty in the predictions inside the valley in Fig. 21 on top of the Northeast ridge.
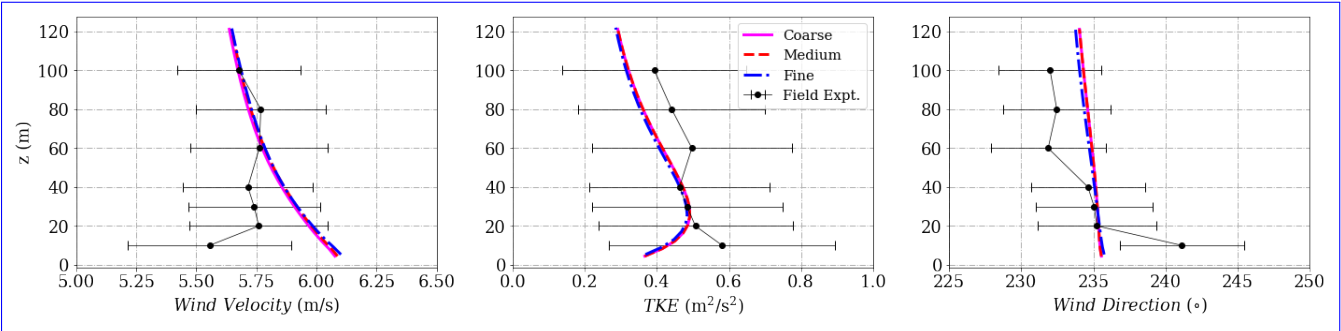
**Figure 19.** Profiles for a) Velocity magnitude b) Turbulent kinetic energy c) Meteorological wind direction at Tower 20 (tse04) on the Southwest ridge, shown for different levels of grid refinement.
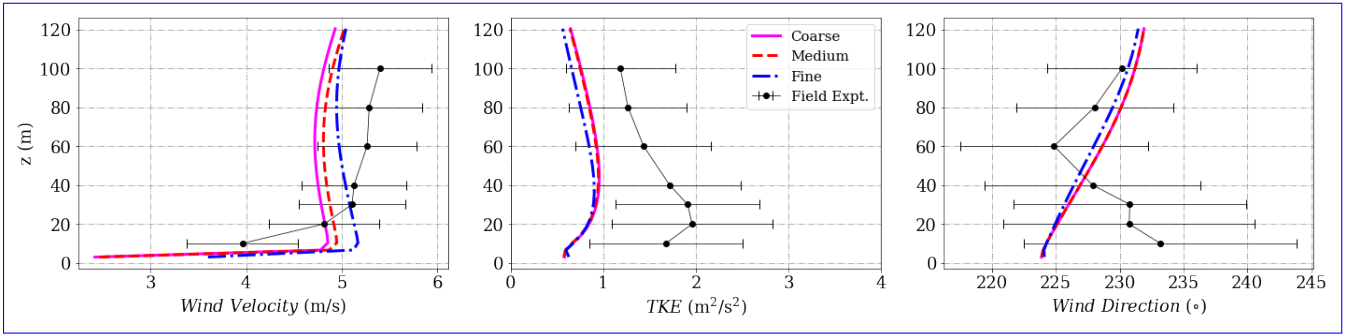
**Figure 20.** Profiles for a) Velocity magnitude b) Turbulent kinetic energy c) Meteorological wind direction at Tower 29 (tse13) on the Northeast ridge, shown for different levels of grid refinement
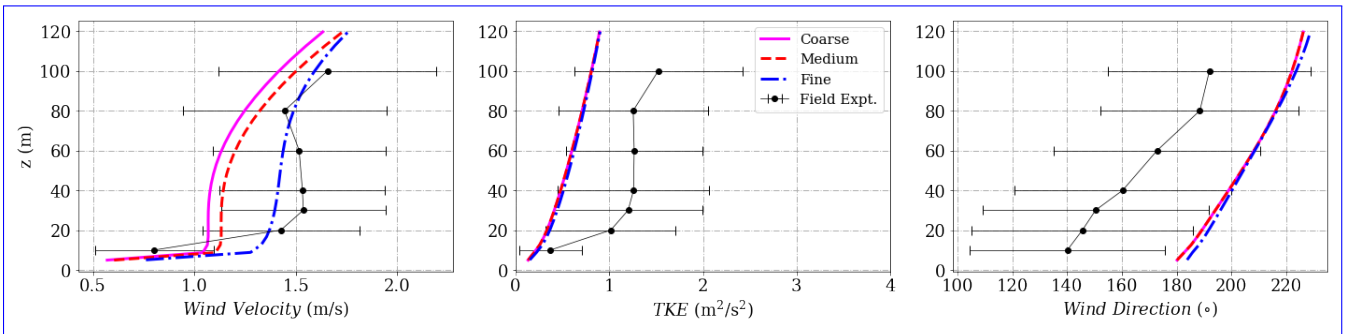
**Figure 21.** Profiles for a) Velocity magnitude b) Turbulent kinetic energy c) Meteorological wind direction at Tower 25 (tse09) inside the valley, shown for different levels of grid refinement

## Inflow profiles - precursor and log-law

Two sets of inflow profiles are utilized as shown in Fig 22. An idealized set of inlet profiles, including a logarithmic velocity profile, and a fully developed profile using a precursor driven by a Coriolis force and a pressure gradient force. The inflow velocity profiles are calibrated to reach the desired inflow conditions at the met-mast Tower 20 at a height 100 m, for a time period identified as neutral based on the Bulk Richardson number. The wind velocity magnitude profiles is close to logarithmic. For the wind direction, the idealized profile fixes a uniform wind direction, but the precursor has source term to account for the Coriolis effect, so a wind veer is seen over the entire height. Finally, for the TKE, a profile is set in the idealized case while for the precursor developed profile it is limited by the maximum mixing length scale, hence there is a decrease in turbulence levels over height.

## Governing equations
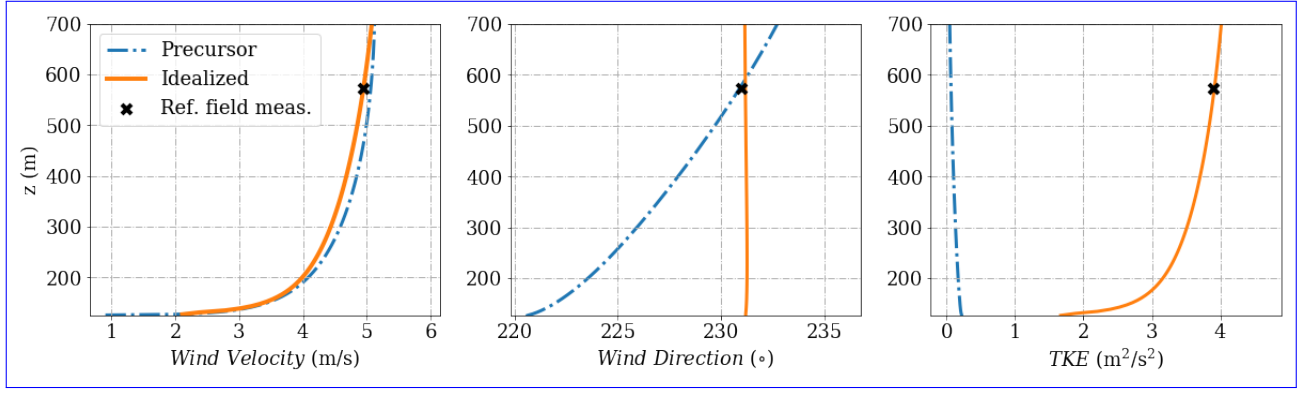
**Figure 22.** Idealized and Precursor (developed) input profiles for a) Wind velocity magnitude b) Wind direction c) Turbulent kinetic energy tuned to reach calibration at height 573 m corresponding to 100 m at Tower 20 (tse04)

The equations solved for the buoyantBoussinesqSimpleFoam solver are the continuity equation (Eqn. 4), momentum equation (Eqn. 5) and turbulence transport (Eqn. 7, 8), temperature (Eqn. 6) as described by Alletto et al. (2018). The pressure gradient ($\pi_i$) drives the momentum equation, the source terms for Coriolis and canopy effects are included in momentum equation. The buoyancy terms are only added in the turbulence transport equations, but are set to zero for the present neutral case. The equation for turbulent dissipation rate contains the maximum length turbulence scale limiter ($l_{max}$) to modify the mixing-length scale estimations for setting different atmospheric stabilities. This description has been added to the Appendix of the manuscript.

$$\frac{\partial \rho \bar{u}_i}{\partial x_i} = 0 \tag{4}$$

$$\frac{\partial \rho \bar{u}_i}{\partial t} + \frac{\partial \rho \bar{u}_i \bar{u}_j}{\partial x_j} - \frac{\partial}{\partial x_j}\left(\rho\left(v + v_t\right)\left(\frac{\partial \bar{u}_i}{\partial x_j} + \frac{\partial \bar{u}_j}{\partial x_i}\right)\right) = -\frac{\partial \bar{p}}{\partial x_i} - \pi_i - \rho \epsilon_{ijk} f_j \bar{u}_k - \rho c_d \Sigma \bar{u}_i |\bar{u}| \tag{5}$$

$$\frac{\partial \rho \bar{\theta}}{\partial t} + \frac{\partial \rho \bar{u}_i \bar{\theta}}{\partial x_i} - \frac{\partial}{\partial x_i}\left(\rho\left(v + \frac{v_t}{\sigma_\theta}\right)\frac{\partial \bar{\theta}}{\partial x_i}\right) = S_\theta \tag{6}$$

$$\frac{\partial k}{\partial t} + \bar{u}_j \frac{\partial k}{\partial x_j} - \frac{\partial}{\partial x_j}\left(\left(v + \frac{v_t}{\sigma_k}\right)\frac{\partial k}{\partial x_j}\right) = P_k - \varepsilon + B \tag{7}$$

$$\frac{\partial \varepsilon}{\partial t} + \bar{u}_j \frac{\partial \varepsilon}{\partial x_j} - \frac{\partial}{\partial x_j}\left(\left(v + \frac{v_t}{\sigma_\varepsilon}\right)\frac{\partial \varepsilon}{\partial x_j}\right) = \left(C_{\varepsilon 1} + (C_{\varepsilon 2} - C_{\varepsilon 1})\left(\frac{l}{l_{\max}}\right)^a\right)\frac{\varepsilon}{k}P - C_{\varepsilon 2}\frac{\varepsilon^2}{k} +$$
$$((C_{\varepsilon 1} - C_{\varepsilon 2})\alpha_B)\frac{\varepsilon}{k}B - (C_{\varepsilon 1} - C_{\varepsilon 2})\frac{\varepsilon}{k}S_d \tag{8}$$